5-2021

Efficient Inversion of 2.5D Electrical Resistivity Data Using the Discrete Adjoint Method

Diego Domenzain
Colorado School of Mines

John Bradford
Colorado School of Mines

Jodi Mead
Boise State University

Efficient inversion of 2.5D electrical resistivity data using the discrete adjoint method

(January 8, 2021)

Running head: **Efficient 2.5D ER inversion**

ABSTRACT

We present a memory and operation-count efficient 2.5D inversion algorithm of electrical resistivity (ER) data that can handle fine discretization domains imposed by other geophysical (e.g, ground penetrating radar or seismic) data. Due to numerical stability criteria and available computational memory, joint inversion of different types of geophysical data can impose different grid discretization constraints on the model parameters. Our algorithm enables the ER data sensitivities to be directly joined with other geophysical data without the need of interpolating or coarsening the discretization. We employ the adjoint method directly in the discretized Maxwell's steady state equation in order to compute the data sensitivity to the conductivity. In doing so, we make no finite difference approximation on the Jacobian of the data and avoid the need to store large and dense matrices. Rather, we exploit matrix-vector multiplication of sparse matrices and find successful convergence using gradient descent for our inversion routine without having to resort to the Hessian of the objective function. By assuming a 2.5D subsurface, we are able to linearly reduce memory requirements when compared to a 3D gradient descent inversion, and by a power of two when compared to storing a 2D Hessian. Moreover, our method linearly outperforms operation counts when compared to 3D Gauss-Newton conjugate-gradient schemes, which

scales cubically in our favor with respect to the thickness of the 3D domain. We physically appraise the domain of the recovered conductivity using a cut-off of the electric current density present in our survey. We present two case studies in order to assess the validity of our algorithm. First, on a 2.5D synthetic example, and then on field data acquired in a controlled alluvial aquifer, where we were able match the recovered conductivity to borehole observations.

INTRODUCTION

Electrical resistivity (ER) inversions that take into account the full response of the observed data without assuming subsurface geometry are useful tools for quantitatively characterizing subsurface properties. Moreover, joining ER data with other geophysical methods can achieve higher accuracy on the recovered parameters. For example, Gallardo and Meju (2003) join ER with travel-time seismic data, and Doetsch et al. (2010) join ER with travel-time ground penetrating radar (GPR) data. Both of the mentioned methods linearize their respective wave propagation method. In doing so, the domain discretization is relaxed. Emerging inversion methods that use the full waveform of the data demand finer discretization constraints (Courant et al., 1967). For example, Domenzain et al. (2020a) join ER with GPR data by solving for the full physical response given by Maxwell's equations in two-dimensional space.

Given that the discretization of the ER governing equations do not require fine grid meshes along the entire computational domain, using second order optimization methods (Kochenderfer and Wheeler, 2019) is common practice in most ER inversion schemes (Loke and Barker, 1996; Oldenburg and Li, 1999; Günther et al., 2006; Pidlisecky et al., 2007). Although useful on ER data, emerging inversion algorithms that join sensitivities from other time domain geophysical methods demand either (i) interpolation of the subsurface parameters or (ii) having both sensitivities on the same computational grid (Domenzain et al., 2020a).

The benefit of joining time-domain methods (such as GPR or seismic) with ER data is twofold, (i) allow the low spatial-frequency of the ER concuctivity solution to constrain the GPR (or seismic) velocity, and (ii) let the high spatial-frequency sensitivity of the GPR

(or seismic data) enhance the ER resolution. Domenzain et al. (2020b) show that both the GPR velocity and ER conductivity recovered parameters can benefit from using structural similarity constraints. They do so by directly joining the full-waveform inversion (FWI) GPR sensitivities with the ER sensitivities. It is worth mentioning that FWI schemes can be computationally demanding both in memory and operation count. Moreover, recent field-data FWI inversions of both GPR (Keskinen et al., 2017; Zhou et al., 2020) and elastic-seismic (Groos et al., 2017; Pan et al., 2019) data assume a 2D subsurface geometry. Even more, most multi-offset GPR surveys also assume a 2D subsurface geometry (Forte and Pipan, 2017). This is due both to acquisition and computation costs. It is therefore desirable to use efficient ER sensitivity computations when joining ER data to an FWI scheme.

In order to motivate the usefulness of our 2.5D ER inversion method, we briefly discuss three possible field scenarios for GPR and elastic-seismic FWI. Ernst et al. (2007) perform 2D FWI of GPR borehole data on an alluvial aquifer, a setting with usual electrical parameters found in the subsurface. Their inversion domain is 8m by 20m, and their slowest velocity is 0.07m/ns. The number of pixels in their domain is roughly 10^5. Groos et al. (2017) use 2D elastic-seismic FWI to solve for both pressure and shear wave velocities. In their work, they consider shear wave velocities as low as 80m/s. We consider a 2D domain 200m in length and 20m in depth with a central frequency of 80Hz. In this case, the number of pixels in the domain is 10^6. Brossier et al. (2009) also perform 2D elastic-seismic FWI on a 20Km by 5Km domain with shear wave velocities as low as 1.2Km/s. Although they perform their inversion in the frequency-domain, we consider the time-domain scenario with a central frequency of 20Hz which yields 10^7 pixels in the domain. Figure 1**a** shows in dashed vertical columns the needed memory for the discussed GPR and elastic-seismic

FWI examples.

Second order optimization methods such as quasi-Newton schemes need to store in memory the Hessian of the objective function. In Figure 1**a** we see in dark gray the amount of double precision memory needed to store the Hessian of the objective function for a range of domain sizes,

$$\text{3D Hessian memory} = (\#\text{ of 2D pixels} \cdot n_y)^2, \tag{1}$$

where *pixels* refers to the discretized grid-nodes of the computational domain, and n_y denotes the number of 2D xz-planes in the y-direction of the 3D discretized domain. Values in Figure 1 are shown for $1 \leq n_y \leq 10^4$. While memory requirements for second order ER inversion schemes are feasible, incorporating time-domain sensitivities from different geophysical methods can drastically increase the amount of memory.

Loke and Barker (1996) and Pidlisecky et al. (2007) approximate the Jacobian of the ER data with a finite difference scheme at each grid point. Alternatively, more efficient adjoint methods give direct access to the sensitivity of the data in the entire computational domain.

Ellis and Oldenburg (1994) and Günther et al. (2006) use the adjoint method for directly computing (and storing) the Jacobian of the data. Marescot et al. (2008) use the adjoint method for computing the gradient of the objective function. All approaches employ a 3D geometry of the subsurface. The approach of Marescot et al. (2008) for computing the gradient involves storing (i) one 3D electric potential, (ii) one 3D forward model matrix and (iii) one 3D adjoint field. Using a rectangular grid, the 3D forward model matrix costs roughly five copies of the domain. In total from (i)-(iii) we have $1 + 5 + 1 = 7$ copies of the

3D domain. The most amount of needed memory is,

$$\text{3D gradient method's memory} = \#\text{ of 2D pixels} \cdot n_y \cdot 7, \tag{2}$$

Figure 1**a** shows in translucent light gray the amount of needed memory for this method with $1 \leq n_y \leq 10^4$.

The adjoint method for computing ER sensitivities can be applied by either considering the continuous objective function (Ellis and Oldenburg, 1994; Günther et al., 2006; Marescot et al., 2008), or the discrete objective function (Tripp et al., 1984; Zhang et al., 1995; Pratt et al., 1998; Ha et al., 2006). Tripp et al. (1984) develop a 2.5D ER inversion using a Gauss-Newton approach. Their method stores the Jacobian of the 2.5D data by numerically integrating a cubic spline interpolation of eight 2D Jacobian matrices. Ha et al. (2006) use the discrete adjoint method similar to Pratt et al. (1998) (in the context of acoustic FWI in the frequency domain) for computing a gradient descent direction in a 2D ER inversion. However, their method does not account for 3D variability of the subsurface. Moreover, their method requires to numerically transform the observed data as an *apparent electric field* and do not account for dissolving boundary conditions in the subsurface.

Ha et al. (2006) count the number of operations for the gradient-descent adjoint method inversion as,

$$\begin{aligned}\text{3D adjoint gradient count} = {} & 2 \cdot n_s \cdot (\ \#\text{ of 2D pixels} \cdot n_y)^3 + \\ & 2 \cdot n_s \cdot (\ \#\text{ of 2D pixels} \cdot n_y)^3,\end{aligned} \tag{3}$$

where n_s denotes the number of source-sink pairs in the survey. The first term counts the computation of the forward model, and the second term the computation of the adjoint field. Figure 1**b** shows in light translucent gray this operation count for $1 \leq n_y \leq 10^4$.

Zhang et al. (1995) present a 3D ER inversion that exploits matrix-vector multiplication

in a Gauss-Newton conjugate-gradient scheme. Similarly, Newman and Hoversten (2000) compute data sensitivities using the adjoint method for controlled source electromagnetic (CSEM) data in the frequency domain. Most notably, their method does not need to store nor directly invert the Hessian of the objective function. Rather, their approximation of the Hessian exploits sparse matrix-vector multiplications, and rely on a conjugate-gradient scheme for computing the model update. This allows their needed memory to be similar to equation 2. However, when the domain and the number of source-sink pairs is large, the conjugate-gradient can impose significantly larger computing times when compared to gradient-descent methods. The computation of the Hessian times a vector involves 6 forward model matrix inversions (without counting the synthetic data and adjoint computations), which at each iteration must be computed approximately 10 times for their conjugate-gradient scheme to converge. In total at each iteration their scheme takes,

$$\begin{aligned}\text{3D adjoint conjugate-gradient count} = 4 \cdot n_s \cdot (\ \#\ \text{of 2D pixels} \cdot n_y)^3 + \\ 6 \cdot 10 \cdot 2 \cdot n_s \cdot (\ \#\ \text{of 2D pixels} \cdot n_y)^3,\end{aligned} \tag{4}$$

where the first term corresponds to computing the gradient, and the second to computing the model update using conjugate-gradient. Figure 1**b** shows in dark gray this operation count for $1 \leq n_y \leq 10^4$.

For our ER adjoint method inversion, we adapt the acoustic FWI of Pratt et al. (1998) to a 2D ER inversion that does not need to transform the observed data into an apparent electric field (Ellis and Oldenburg, 1994; Zhang et al., 1995; Domenzain et al., 2020a). Using the approximation of Pidlisecky and Knight (2008), we approximate the 3D subsurface with a linear combination of 2D electric potentials for a 2.5D solution. This linear combination in the continuous case is the inverse Fourier transform in the k_y domain of the 3D solution, which is the physically accurate 2.5D solution. We then use this 2.5D electric potential

approximation to compute the 2.5D conductivity sensitivity as a linear combination of the 2D sensitivities. We use a gradient descent algorithm which relieves the need to store the Jacobian of the data (by exploiting sparse matrix-vector multiplication), or approximate the Hessian of the objective function. Furthermore, assuming a 2.5D subsurface enables us to further reduce memory requirements compared to 3D adjoint methods using gradient descent (Marescot et al., 2008). For our 2D forward model we use dissolving boundary conditions in the subsurface (Dey and Morrison, 1979) which relaxes the need to do extra padding of the domain.

At most, the amount of memory for computing the 2.5D ER sensitivities with our method is given by the memory needed to store (i) the 2D electric potentials, (ii) one 2D adjoint field, and (iii) one 2D forward model matrix. We use four 2D electric potentials as Pidlisecky and Knight (2008). Using a rectangular grid discretization, each forward model matrix costs roughly five copies of the domain. In total from (i)-(iii) we have 4+1+5=10 copies of the domain,

$$\text{Our 2.5D method's memory} = \#\text{ of 2D pixels} \cdot 10. \tag{5}$$

Figure 1**a** shows in black the amount of memory needed with our method for a range in domain size. Our use of the adjoint method and the 2.5D approximation exponentially outperforms memory requirements for the 2D and 3D Hessian. Compared to storing the 2D Jacobian of the data (of size # of pixels $\times$ # of data points) our algorithm costs significantly less memory when the number of data points is larger than 10. Moreover, a linear gain in memory is achieved when compared to the 3D gradient adjoint method. In this case the amount of memory gained is $n_y \cdot 7/10$.

We use a similar version of equation 3 to count the operations needed in our method.

However, we use $n_y = 1$ since our computations are only in the 2D domain. We then multiply for the four copies of our 2D domain that are needed to approximate the 2.5D subsurface,

$$\text{Our 2.5D method's count} = 16 \cdot (\ \#\ \text{of 2D pixels})^3. \tag{6}$$

Figure 1**b** shows in solid black our method's operation count. We note a linear gain in operation count by a factor of n_y^3 for both the 3D adjoint conjugate-gradient and the 3D adjoint gradient methods.

In Table 1 we show specific values of how much memory is needed for each relevant field data example considered, and for each method in Figure 1**a**. Assuming a 2.5D subsurface geometry, an increase of less than an order of magnitude from the best 2D scenario gives a more accurate physical model with our 2.5D method. Converseley, up to 4 orders of magnitude can be gained with our method when compared with the least memory consuming 3D method. In Table 2 we show the operation counts taken from Figure 1**b** along the dotted line, wich marks the fixed number of source-sink pairs we used in our field data example. We again note a benefit for using our 2.5D method. In this case, the cost against 2D is still less than an order of magnitude, while the gain from using a 3D method is more than one order of magnitude in operation count.

Given the low memory storage and modest operation count, our algorithm can be used for joint inversion with data whose forward models impose finer grid constraints without the need to interpolate the parameters, and with less computation cost than using a 3D method.

We assess the accuracy of the recovered conductivity at depth using a measure of electric current density in our survey throughout all iterations. Our method relies on the physical

principle that the sensitivity of surface acquired ER data is given by electric current lines that return to the surface. Although other methods exist (Oldenburg and Li, 1999) and have been successful in field surveys (Oldenborger et al., 2007b), they are costly to compute because more than one inversion is needed for their construction. However, the (costly) exploration of the parameter space given by multiple inversions of the data give a reliable region for appraising the solution. Rather than presenting a substitute for existing methods, we present ours as a computationally cheap alternative that takes into account the physics of the ER survey and the different sensitivities of the data throughout the inversion. We show that at worst our approach is conservative in appraising the solution domain.

We show the usefulness of our work with a synthetic example and field data acquired at an alluvial aquifer near Boise, Idaho USA. Both experiments consist of only surface acquired ER data. We perform our inversions on finely discretized grids where each pixel is square and of side-length equal to 0.05m. These discretization values comply with numerical stability criteria for a GPR 2D full-waveform inversion on commonly encountered scenarios. For example Ernst et al. (2007) use a 0.14m spacing for their inversion and 0.04m for their forward modeling on the same alluvial aquifer. Furthermore, the physical size of our entire domain for the ER field data inversion is also relevant for GPR exploration (15m in depth and 45m across). This enables our algorithm to potentially join ER and GPR sensitivities of the subsurface without the need for interpolating their respective domains. We compare our results with previous borehole low frequency conductivity studies at the same site (Oldenborger et al., 2007a; Mwenifumbo et al., 2009) and find similar results for petrophysical parameters and conductivity values.

Lastly, we compare our finely recovered conductivity with that of the commercially available software Res2DInv (Loke, 2006) on the smallest possible horizontal grid-size allowed by

the software. While both conductivities exhibit similar features, our algorithm is capable of handling grid-sizes of at least an order of magnitude smaller.

METHODS

ER 2D forward model

Assuming Ohm's law, the two-dimensional physics of the ER experiment are given by the steady state Maxwell's equations (Pidlisecky et al., 2007),

$$-\nabla \cdot \sigma(x,z)\nabla\varphi(x,z) = \underbrace{\mathbf{i}(\delta(x-s_+)-\delta(x-s_-))}_{s(x,z)}, \tag{7}$$

where φ is the electric potential, $\mathbf{i}$ is the current intensity, $s_\pm$ is the source-sink location, and σ is the electrical conductivity. Since we are assuming a 1D survey line perpendicular to the y axis, the source term s does not depend on y. Moreover, because we are considering source-sink locations only at the surface ($z = 0$) the source and sink locations (s_+ and s_-) only depend on x.

We discretize equation 7 using a finite-volume method with Neumann and Robin boundary conditions at the air-ground interface and in the subsurface respectively. The discretization is adapted from Dey and Morrison (1979) for our two-dimensional case. We express our discretization as a matrix-vector product,

$$\begin{aligned} \mathbf{L}\boldsymbol{\varphi}_{2D} &= \mathbf{s}, \\ \mathbf{d}_{2D} &= \mathbf{M}\boldsymbol{\varphi}_{2D}, \end{aligned} \tag{8}$$

where $\mathbf{L}$ is the discretized differential operator of equation 7, $\boldsymbol{\varphi}_{2D}$ is the 2D electric potential, $\mathbf{s}$ is the source term, $\mathbf{M}$ is the measuring operator that computes observed voltages, and $\mathbf{d}_{2D}$ is the data of the experiment for one source-sink location. For every pixel in the domain,

the matrix $\mathbf{L}$ has as many non-zero entries as neighbors and another entry for itself. Since an inner pixel has four neighbors, an upper bound for the non-zero bands of $\mathbf{L}$ is five, with each band having as many elements as pixels are in the domain.

Inversion of 2D ER data

In this section we follow Domenzain et al. (2020a) and briefly review the two-dimensional discrete adjoint method. In section **Inversion of 2.5D ER data** we will generalize this method for our 2.5D solution. We optimize the objective function

$$\Theta_{2D}(\boldsymbol{\sigma};\, \mathbf{d}^o_{2D}) = ||\underbrace{\mathbf{d}_{2D} - \mathbf{d}^o_{2D}}_{\mathbf{e}_{2D}}||^2_2, \tag{9}$$

with respect to the conductivity where $\mathbf{e}_{2D}$ is the residual of the data in two-dimensional space. Domenzain et al. (2020a) show that the gradient $\mathbf{g}_{2D}$ of the objective function Θ_{2D} with respect to $\boldsymbol{\sigma}$ for one source can be expressed as,

$$\begin{aligned} \mathbf{L}^\top \mathbf{v}_{2D} &= \mathbf{M}^\top \mathbf{e}_{2D} \\ \mathbf{g}_{2D} &= \mathbf{S}\, \mathbf{v}_{2D}, \end{aligned} \tag{10}$$

where,

$$\mathbf{S} = -\left((\nabla_\sigma \mathbf{L})\boldsymbol{\varphi}_{2D}\right)^\top, \tag{11}$$

is a sparse banded matrix whose entries are explicitly calculated. Equations 10 and 11 can also be expressed as,

$$\begin{aligned} \mathbf{g}_{2D} &= \mathbf{J}^\top_{2D}\, \mathbf{e}_{2D}, \\ \mathbf{J}_{2D} &= \mathbf{M}\mathbf{L}^{-1}\mathbf{S}^\top. \end{aligned} \tag{12}$$

We note that because we are computing the derivative with respect to $\boldsymbol{\sigma}$ on the discrete operator $\mathbf{L}$, the boundary conditions of $\mathbf{L}$ are also taken into account in $\mathbf{S}$. The number of non-zero entries in $\mathbf{S}$ is the same as $\mathbf{L}$. Each column of $\mathbf{S}$ accounts for one virtual source

(Pratt et al., 1998; Ha et al., 2006) and in a given iteration it is computed once per source **s**.

ER 2.5D forward model

Equation 7 disregards the 3D nature of the earth that is present in field data. In order to account for 3D structure while still assuming no significant change in the y direction, we can express the governing physics of the ER experiment as

$$-\nabla \cdot \sigma(x,z)\nabla\,\varphi(x,y,z) = s(x,z). \tag{13}$$

In order to solve equation 13 we use the Fourier-cosine transform in the k_y-domain (Pidlisecky and Knight, 2008),

$$-\nabla \cdot \sigma\nabla\,\tilde{\varphi}(x,k_y,z) + k_y^2\,\sigma\,\tilde{\varphi}(x,k_y,z) = \frac{1}{2}s(x,z), \tag{14}$$

and then use the inverse Fourier-cosine transform to get the electric potential solution in the xz-plane,

$$\varphi(x,y=0,z) = \frac{2}{\pi}\int_0^\infty \tilde{\varphi}\,\mathrm{d}k_y. \tag{15}$$

As explained by Pidlisecky and Knight (2008), discretizing equation 15 amounts to optimizing for an array $\boldsymbol{k}$ of k_y values and a corresponding array $\boldsymbol{\omega}$ of weights ω. For completeness, we include the details of this optimization in Appendix **A**. Both $\boldsymbol{k}$ and $\boldsymbol{\omega}$ do not depend on the subsurface conductivity. They only depend on the source-receiver geometry.

Once $\boldsymbol{k}$ and $\boldsymbol{\omega}$ have been computed, we discretize equation 14 for each weight k_i in $\boldsymbol{k}$ as,

$$\mathbf{L}_i = \mathbf{L}^i + k_i^2\,\boldsymbol{\sigma}, \tag{16}$$

where $\mathbf{L}^i$ is very similar as in equation 8 but the Robin boundary conditions in the subsurface are now different, as dictated by equation A-2. The ith 2D forward model is,

$$\begin{aligned} \mathbf{L}_i\tilde{\boldsymbol{\varphi}}_i &= \frac{\mathbf{s}}{2}, \\ \tilde{\mathbf{d}}_i &= \mathbf{M}\tilde{\boldsymbol{\varphi}}_i. \end{aligned} \tag{17}$$

The full 2.5D forward model, i.e. the discretized expression of 15 is,

$$\boldsymbol{\varphi} = \frac{2}{\pi}\sum_i \tilde{\boldsymbol{\varphi}}_i\,\omega_i. \tag{18}$$

In Figure 2 we give all the steps of the algorithm for computing $\boldsymbol{\varphi}$.

Inversion of 2.5D ER data

Now that we have formulated the 2D gradient computation (see equation 10) and the 2.5D forward model (see equations 17 and 18), we explain how to compute the 2.5D gradients for a 2.5D conductivity solution. We now want to optimize the objective function

$$\Theta(\boldsymbol{\sigma};\,\mathbf{d}^o) = ||\underbrace{\mathbf{d}-\mathbf{d}^o}_{\mathbf{e}}||_2^2, \tag{19}$$

with respect to the conductivity where $\mathbf{e}$ is the residual of the data in 2.5 dimensional space. We compute the gradient $\mathbf{g}$ of Θ by,

$$\mathbf{g} = \mathbf{J}^\top\mathbf{e}, \tag{20}$$

where $\mathbf{J} = \nabla_\sigma\mathbf{d}$. The gradient operator ∇_σ is a row vector with the ith entry being the partial derivative ∂_{σ_i}. In order to find an expression for $\mathbf{J}$ we first write $\mathbf{d}$ in terms of $\tilde{\mathbf{d}}_i$,

$$\mathbf{d} = \mathbf{M}\boldsymbol{\varphi} = \mathbf{M}\underbrace{\frac{2}{\pi}\sum_i \omega_i\tilde{\boldsymbol{\varphi}}_i}_{\boldsymbol{\varphi}}, = \frac{2}{\pi}\sum_i \omega_i\underbrace{\mathbf{M}\tilde{\boldsymbol{\varphi}}_i}_{\tilde{\mathbf{d}}_i} = \frac{2}{\pi}\sum_i \omega_i\tilde{\mathbf{d}}_i. \tag{21}$$

We can now apply ∇_σ to equation 21,

$$\nabla_\sigma \mathbf{d} = \frac{2}{\pi} \sum_i \omega_i \underbrace{\nabla_\sigma \tilde{\mathbf{d}}_i}_{\mathbf{J}_i} = \underbrace{\frac{2}{\pi} \sum_i \omega_i \mathbf{J}_i}_{\mathbf{J}}, \tag{22}$$

Equation 22 is a recipe for computing $\mathbf{J}$. By substituting equation 22 in equation 20 we have,

$$\begin{aligned} \mathbf{g} &= \frac{2}{\pi} \left(\sum_i \omega_i \mathbf{J}_i \right)^\top \mathbf{e} \\ &= \frac{2}{\pi} \sum_i \omega_i \underbrace{\mathbf{J}_i^\top \mathbf{e}}_{\tilde{\mathbf{g}}_i}. \end{aligned} \tag{23}$$

In the last equality we write $\tilde{\mathbf{g}}_i = \mathbf{J}_i^\top \mathbf{e}$ because with a similar approach as equation 10, from equation 17 we have,

$$\begin{aligned} \mathbf{L}_i^\top \tilde{\mathbf{v}}_i &= \mathbf{M}^\top \mathbf{e}, \\ \tilde{\mathbf{g}}_i &= \mathbf{S}_i \tilde{\mathbf{v}}_i, \end{aligned} \tag{24}$$

where

$$\mathbf{S}_i = -\left((\nabla_\sigma \mathbf{L}^i) \tilde{\boldsymbol{\varphi}}_i \right)^\top - k_i^2 \, \mathrm{diag}(\tilde{\boldsymbol{\varphi}}_i)^\top, \tag{25}$$

and similarly to equation 12 we have $\mathbf{J}_i = \mathbf{M}\mathbf{L}_i^{-1}\mathbf{S}_i^\top$. In conclusion, we compute the gradient $\mathbf{g}$ of equation 19 by,

$$\mathbf{g} = \frac{2}{\pi} \sum_i \omega_i \tilde{\mathbf{g}}_i. \tag{26}$$

Figure 3 gives a summary for computing $\mathbf{g}$.

Updating the conductivity

Equation 26 gives the gradient $\mathbf{g}$ for equation 19 with respect to $\boldsymbol{\sigma}$ for one source. We regularize $\mathbf{g}$ by adding the normalized residual of a reference conductivity $\boldsymbol{\sigma}_o$ and then smoothing in the space-frequency domain. After computing $\mathbf{g}$ with equation 26 and normalizing by its

largest magnitude we have,

$$\mathbf{g} \leftarrow \mathbf{g} + \beta \frac{\boldsymbol{\sigma} - \boldsymbol{\sigma}_o}{\max(\mathrm{abs}(\boldsymbol{\sigma} - \boldsymbol{\sigma}_o))}, \tag{27}$$

where β is a fixed number smaller than one. The gradient $\mathbf{g}$ exhibits large values near the receiver locations. In order to suppress these artifacts, we smooth $\mathbf{g}$ using a space-frequency low-pass filter (Taillandier et al., 2009; Groos et al., 2017; Domenzain et al., 2020a). In practice we use a gaussian of width λ,

$$\lambda = \frac{1}{\Delta r \cdot a}, \tag{28}$$

where Δr is the minimum electrode spacing in meters and a is close to one, loosely $0.5 \leq a \leq 1.5$. Although similar to the conventional spatial-derivative matrix used for smoothing data sensitivities, this approach proves more effective in removing receiver artifacts when using the adjoint method. As with any smoothing or regularization operator, a compromise is made between spatial resolution of the solution and the resulting fit to the data. Ideally, a filter of width $1/\Delta r$ should suffice. However, as with any regularization parameter, λ depends on the true subsurface parameters and the initial conductivity model. Therefore, a fixed value of λ ranging more and less than $1/\Delta r$ has to be found for each specific case.

In order to enforce positivity constraints on $\boldsymbol{\sigma}$ we do a logarithmic change of variable on the objective function $\Theta(\boldsymbol{\sigma}) = \Theta(\ln(\boldsymbol{\sigma}))$ (Meles et al., 2010). Using the chain rule we have,

$$\mathbf{g}_{\boldsymbol{\sigma}} = \frac{1}{\boldsymbol{\sigma}} \odot \mathbf{g}_{\ln \boldsymbol{\sigma}}, \tag{29}$$

where the subscript denotes the variable under consideration and $\odot$ denotes element wise multiplication. Computing the update, using equation 29 and taking the inverse of the logarithm we have,

$$\begin{aligned} \ln(\boldsymbol{\sigma}_{i+1}) &= \ln(\boldsymbol{\sigma}_i) - \alpha\, \mathbf{g}_{\ln \boldsymbol{\sigma}}, \\ \boldsymbol{\sigma}_{i+1} &= \boldsymbol{\sigma}_i \odot \exp(-\alpha \cdot \boldsymbol{\sigma}_i \odot \mathbf{g}_{\boldsymbol{\sigma}}). \end{aligned} \tag{30}$$

Equation 30 holds true for one source-sink location. In practice however, we update $\boldsymbol{\sigma}$ once all update directions $-\alpha\mathbf{g}$ for all sources in our survey have been computed. The step-size α is found as proposed by Pica et al. (1990) and adapted for our ER inversion by Domenzain et al. (2020a). This step-size computation also constraints the range of possible values for $\boldsymbol{\sigma}$ by an arbitrary user defined interval. In practice, we define this interval by the minimum and maximum values of the observed apparent resistivities. The entire process of computing the step-size only costs one 2.5D forward model computation.

The global update $\Delta\boldsymbol{\sigma}$ is the average of all update directions over all source-sink pairs. At late iterations when the sensitivity of our data is weak, $\Delta\boldsymbol{\sigma}$ might struggle to find a true descent direction. This issue can be addressed by using *momentum* (Rumelhart et al., 1986) which only costs the storage of the previous iteration update, $\Delta\boldsymbol{\sigma}_\bullet$. The final update for the conductivity is given by,

$$\begin{aligned} \Delta\boldsymbol{\sigma} &\leftarrow \Delta\boldsymbol{\sigma} + \beta_\bullet \Delta\boldsymbol{\sigma}_\bullet, \\ \boldsymbol{\sigma} &\leftarrow \boldsymbol{\sigma} \odot \exp(\boldsymbol{\sigma} \odot \Delta\boldsymbol{\sigma}), \end{aligned} \tag{31}$$

where $\beta_\bullet$ is a fixed number smaller than one. Figure 4 gives the full algorithm for our inversion.

Solution appraisal

Physically, the sensitivity at depth of the ER survey is related to the electric current density of all source-sink pairs in the survey. Depending on our initial model, each forward model in the ER inversion might have different electric current densities throughout iterations. Therefore, throughout the inversion the illumination of the subsurface changes as a function of the observed data and the initial conductivity model.

At each iteration i, we quantify the total electric current density in our inversion by summing the absolute value of the electric potentials $\boldsymbol{\varphi}$ given by our forward models (see equation 18),

$$\Psi_i = \sum_j |\boldsymbol{\varphi}_j|, \tag{32}$$

where j runs through all forward models. As iterations proceed, we keep adding the previous Ψ_i to the new one to obtain a final measure of electric current density Ψ, then we normalize Ψ by its largest amplitude,

$$\begin{aligned} \Psi &= \sum_i \Psi_i \\ \Psi &\leftarrow \frac{\Psi}{\max(\Psi)}. \end{aligned} \tag{33}$$

Given the harmonic nature of the electric potential, the field Ψ will have a level curve beyond which the electric current lines will no longer return to the surface. We choose this level curve as a cut-off for Ψ from which all level curves below this cut-off are considered to not contain relevant information. The resulting image for Ψ is then a collection of ones in the xz-plane above the cut-off value.

EXAMPLES

In this section we verify the validity of our algorithm on two scenarios: a synthetic 2.5D example, and on field data aquired in a controlled alluvial aquifer.

Synthetic data example

We test our algorithm on a synthetic scenario as shown in Figure 5**a**. The model consists of a 20m by 4m subsurface domain with a 10mS/m cylindrical anomaly embedded in a 5mS/m background. We use 17 electrodes spaced 1m apart with all possible dipole-dipole, Wenner

and Schlumberger arrays. The full discretized domain is of size 81×401 with a square pixel size of 0.05m.

Our initial model is a homogeneous conductivity equal to the background of our model. Besides smoothing the gradients $\mathbf{g}$, for this example we do not impose regularization on the inversion. We choose a smoothing factor of $a = 1.1$ (see equation 28) and a value of $\beta_\bullet = 0.02$.

In Figure 5**b** we see the recovered conductivity in the entire computational domain, and in Figure 5**c** we see the recovered conductivity with a current density cut-off of 0.025% of the maximum value of Ψ (see equation 33). Our solution appraisal technique is able to remove parts of the domain where we have a poor constraint in our solution (bottom of the domain) but keep parts where the recovered conductivity remains close to the true model. We note that by choosing a cut-off that eliminates the electric current leaving the domain, we are conservatively assessing our solution.

Field data example

We acquired field data at the Boise Hydrological Research Site (BHRS) in May 2019. The site is an alluvial aquifer next to the Boise river as seen in Figure 6 (modified from Barrash et al. (1999)). The water flow in the river is controlled by a nearby dam and is increased throughout spring as warmer temperatures thaw the snowpack in the nearby Sawtooth mountain range (Barrash et al., 1999). We aimed our experiment to take place when the water table was at its highest point without the site being flooded. This choice was made to increase the electric current of our survey past the water table boundary and improve our depth sensitivity. We used an *IRIS Syscal Pro* resistivity system with a total of 36

electrodes spaced 1m apart in a one dimensional line perpendicular to the river as shown in Figure 6. Our survey consisted of all possible dipole-dipole and Wenner arrays for a total of 1175 source-receiver pairs. Although approximately planar, the ground surface dips slightly (0.4m over 36m) toward the river.

Based on knowledge of site stratigraphy (e.g. Bradford et al. (2009)) the position of the line perpendicular to the river was chosen to enhance the variability of conductivity in the xz-plane while keeping the y coordinate variability of the conductivity approximately constant. For each source-receiver pair the raw data recorded by the Syscal Pro is in units of volts, paired with readings of source current magnitude (positive and in units of Amperes), apparent resistivites computed by the system (in units of Ohm per meter), and a measure of standard deviation (each source was performed eight times).

Preprocessing

For our inversion we use only the voltage readings. However, before performing our inversion we use all the Syscal Pro data to enhance the quality of our inversion in three steps. 1) Remove the negative apparent resistivities given by the Syscal Pro system since these data points are not physical and are contaminated by noise. 2) Eliminate data points whose standard deviation is more than a fixed cut-off. In this case the cut-off was 5 standard deviations. 3) Divide the voltage readings by their respective source current magnitude. This last step is done to enable multi source-receiver pairs in each forward model of our inversion. Our data consists of 342 different source-sink positions and a total of 1175 data points. The next step is to compute the weights $\boldsymbol{k}$ and $\boldsymbol{\omega}$ (see Figure A-1). Figure 7**a** and Figure 8**a** give the observed but preprocessed apparent resistivities of the dipole-dipole with

a-spacing equal to 1m and Wenner arrays respectively.

Inversion

Our initial model is a homogeneous subsurface with conductivity equal to 2mS/m. We regularize the inversion using a homogeneous reference conductivity equal to our initial model, and weighting factors of $\beta = 0.001$ and $\beta_\bullet = 0.5$. The full discretized domain is of size 301×901 with a square pixel size of 0.05m, i.e. 15m deep and 45m across. Figure 9 gives the recovered conductivity corrected for topography and with a current density cut-off equal to 0.002%. Figure 10 shows the observed vs recovered data.

We evaluate our results with water table depth, neutron porosity (Barrash and Clemo, 2002), and capacitive conductivity (Mwenifumbo et al., 2009) taken from borehole measurements. For our borehole analysis we choose to use the full domain of our solution. We do this because as explained below we are still able to extract meaningful physical information of the subsurface, and as noted in the synthetic example, our cut-off criteria can be overly conservative. The water table depth was 1m and measured the same day the survey was done. Figure 9 shows our recovered conductivity accurately images the water table boundary. We further note the higher conductivity, sand filled paleo channel that deepens toward the river is accurately represented.

Figure 11 shows the normalized porosity and recovered conductivity along the entire computational domain. Qualitatively, our recovered conductivity and measured porosity follow the same low-frequency trend. This trend is mostly appreciated in Figure 11**a** for borehole B5, where the peak-trough-peak shape of the porosity is closely followed by the recovered conductivity beyond our solution appraisal cut-off.

Quantitatively, we compare our inversion results following Oldenborger et al. (2007a) who perform a time lapse borehole ER monitoring of the same site in Summer of 2004. Their analysis uses Archie's law (Archie et al., 1942) to compare the formation factor derived by ER recovered conductivity and the formation factor derived by the neutron porosity. For each borehole B5, A1 and B2 we compute the formation factor with our recovered conductivity,

$$F_{ER} = \frac{\sigma_f}{\boldsymbol{\sigma}_z}, \tag{34}$$

where $\boldsymbol{\sigma}_z$ denotes our recovered conductivity along the borehole and σ_f is the fluid conductivity. We take $\sigma_f = 20$mS/m as given by Oldenborger et al. (2007a). We then invert in depth for the cementation factor m using the neutron porosity ϕ and the porosity derived from F_{ER},

$$\phi_{ER} = \left(\frac{1}{F_{ER}}\right)^{1/m}. \tag{35}$$

This gives us a depth profile for m. Using m we compute the formation factor from the neutron porosity as,

$$F_\phi = \frac{1}{\phi^m}. \tag{36}$$

Oldenborger et al. (2007a) give average values of $F_{ER} = 13 \pm 4$, $m = 1.7$ and $F_\phi = 13 \pm 4$. In Table 3 we find similar values (within ± 1 standard deviation) for F_{ER}, F_ϕ and m with our recovered conductivity.

Figure 12 shows our recovered conductivity next to the capacitive conductivity as measured by Mwenifumbo et al. (2009). Their experiment was performed in the month of November, when the river water flow had significantly decreased to a 2m deep water table. Even though our experiments were performed with different ground water conditions, our recovered conductivity is within the same order of magnitude and follows close resemblance

inside our appraised solution. Beyond our appraised solution near 10m in depth, both conductivity profiles show an up-ward trend that is also present in the neutron porosity (Figure 11).

Lastly, we compare our recovered conductivity with the result of the commercial software Res2DInv in Figure 13. Although the purpose of Res2DInv is not to recover subsurface conductivity on a very fine discretized domain, we choose to compare our results to this software because of its wide use in the geophysics community. Res2DInv uses a Gauss-Newton minimization scheme which stores an approximation of the Hessian at each iteration (Sasaki, 1992; Loke and Barker, 1996; Loke, 2006). The amount of memory needed for this method is shown in dark grey in Figure 1**a** as a function of domain size, and in Table 1 for different domain sizes based on relevant field data scenarios. In their manual (Loke, 2006) it is noted that a fine discretization can significantly increase memory requirements and is not recommended. The inversion parameters for the Res2DInv result were taken equal to those of our inversion: minimizing the L2 norm and a reference conductivity model of 2mS/m weighed by a regularization parameter of 0.001. The horizontal grid-size for the Res2DInv result was chosen as the minimum possible value allowed by the software, which is half the receiver spacing (in this case 0.5m). The vertical grid-spacing was chosen to be 0.25m and the entire computational domain was set to the full rectangular xz-plane.

We note that both results in Figure 13 follow the same low spatial-frequency trend: the water table is placed at approximatelly the same depth and the sand channel exhibits a similar shape. However, the scheme used by Res2DInv fails to comply with time-domain finely discretized domains.

CONCLUSIONS

We have developed an efficient discrete adjoint based method for inverting 2.5D electrical resistivity (ER) data. We directly obtain the sensitivity of the data in the entire domain and do not need to approximate the Jacobian of the data using finite differences. Moreover, we take into account dissipating boundary conditions in the subsurface and do not need to store large dense matrices (like the Jacobian of the data and the Hessian of the objective function). In geologic scenarios where a 2.5D subsurface holds true, our algorithm linearly outperforms memory requirements for 3D gradient descent adjoint methods. Compared to computing the 2D Jacobian of the data, our 2.5D algorithm is also linearly less memory intensive. Moreover, compared to storing a 2D Hessian matrix our algorithm uses exponentially less memory. Regarding operation count, our algorithm linearly outperforms 3D Gauss-Newton conjugate-gradient schemes by a factor equal to the cubed width of the 3D domain.This enables us to very finely discretize the subsurface with feasible memory requirements and a modest operation count. As a result, our algorithm can be used for joint inversion with data whose forward models impose finer grid constraints (for example, ground penetrating radar) without the need to interpolate the model parameters.

Regarding field-relevant applications that aim to join time-domain methods, our algorithm provides a memory gain of 4 orders of magnitude over the cheapest 3D inversion method (which is the 3D extension of the method presented here), and only a linear increase in memory over the cheapest 2D inversion method. Looking ahead as computational 3D capabilities become ever more possible, our algorithm can still provide an efficient alternative for 2.5D solutions.

The practical utility of our work lies in improving the efficiency and resolution of ER

methods in application of joint inversions with 2.5D FWI-GPR and other geophysical data. It is a good stand alone inversion tool in settings where the 2.5D approximation for real earth geology is valid.

In order to assess the quality of the recovered parameters, we use a measure of the electric current density present in our domain throughout iterations. This method for quality assessment takes into account the physics of the ER survey, the data, the model parameters throughout iterations and does not need extra inversions with different initial models. At worst our method is conservative in assessing the quality of the recovered parameters. However, it is less accurate than other existing methods that explore the model space in a more exhaustive way.

We tested our algorithm on a synthetic example and on field data acquired at an alluvial aquifer near Boise, Idaho USA. Our inversions were done on a finely discretized grid where each square pixel had 0.05m in side-length. These discretization values comply with numerical stability requirements for ground penetrating radar (GPR) 2D full-waveform inversion on the same field site, and common geologic scenarios. Moreover, the field data inversion was performed on a domain of size relevant for GPR exploration of the subsurface (15m deep and 45m in length). Such a fine discretization is not supported in widely used commercially available software. This enables our algorithm to directly join the ER sensitivity of the subsurface with GPR sensitivities without the need to interpolate the domain. We find good correlation of our field data results with neutron porosity and capacitive conductivity borehole measurements taken on the site in previous surveys.

APPENDIX A

FOURIER COEFFICIENTS FOR 2.5D TRANSFORM

In order to solve equation 18 we must find weights $\boldsymbol{k}$ and $\boldsymbol{\omega}$ to accurately approximate the integral in equation 15. We follow Pidlisecky and Knight (2008) and note that the Green's function solution for homogeneous σ of equation 13 on the half xz-plane is,

$$\varphi(x, y=0, z) = \frac{\mathbf{i}}{2\pi\sigma} \underbrace{\left(\frac{1}{\underbrace{||x - s_+||_2}_{r+}} - \frac{1}{\underbrace{||x - s_-||_2}_{r-}} \right)}_{1/R}. \tag{A-1}$$

Applying the forward Fourier-cosine transform,

$$\tilde{\varphi} = \int_0^\infty \varphi \, \cos(y\, k_y) \, \mathrm{d}y = \frac{\mathbf{i}}{2\pi\sigma}(B_o(k_y r_+) - B_o(k_y r_-)), \tag{A-2}$$

where B_o is the zero order modified Bessel function of the second kind. By plugging in equations A-1 and A-2 into equation 18 we discretize by

$$\begin{aligned} 1 &\approx \sum_j \underbrace{\frac{2R}{\pi}\{B_o(k_j\, r_+) - B_o(k_j\, r_-)\}}_{K_{ij}} \omega_j \\ \boldsymbol{K} &= \frac{2R}{\pi}\left\{B_o(\boldsymbol{k}\, r_+) - B_o(\boldsymbol{k}\, r_-)\right\} \\ \boldsymbol{f} &\approx \boldsymbol{K}\boldsymbol{\omega}, \end{aligned} \tag{A-3}$$

where $\boldsymbol{K} = \boldsymbol{K}(\boldsymbol{k}, \mathbf{s})$ is a matrix of size $n_R \times n_k$, n_R and n_k are the size of R and $\boldsymbol{k}$ respectively, $\boldsymbol{f}$ is a vector of length n_R whose entries should approximate 1, and $\boldsymbol{k} = (k_{yi})$, $\boldsymbol{\omega} = (\omega_i)$ are vectors of length n_k. We minimize

$$\Phi(\boldsymbol{k}) = ||1 - \underbrace{\boldsymbol{K}\underbrace{(\boldsymbol{K}^\top \boldsymbol{K})^{-1}\boldsymbol{K}^\top}_{\boldsymbol{\omega}}}_{\boldsymbol{f}(\boldsymbol{k})}||_2^2 = ||\mathbf{1} - \boldsymbol{f}(\boldsymbol{k})||_2^2, \tag{A-4}$$

using a regularized Newton method. The vector of all ones is denoted $\mathbf{1}$. Note that both $\boldsymbol{k}$ and $\boldsymbol{\omega}$ are geometry dependent and not parameter dependent. Lastly, we follow Pidlisecky

and Knight (2008) and use a small number for n_k, usually $n_k = 4$. Figure gives the full optimization algorithm (Pidlisecky and Knight, 2008) for computing $\boldsymbol{k}$ and $\boldsymbol{\omega}$.

REFERENCES

Archie, G. E., et al., 1942, The electrical resistivity log as an aid in determining some reservoir characteristics: Transactions of the AIME, **146**, 54–62.

Barrash, W., and T. Clemo, 2002, Hierarchical geostatistics and multifacies systems: Boise hydrogeophysical research site, boise, idaho: Water Resources Research, **38**, 14–1.

Barrash, W., T. Clemo, and M. D. Knoll, 1999, Boise hydrogeophysical research site (bhrs): objectives, design, initial geostatistical results: Symposium on the Application of Geophysics to Engineering and Environmental Problems 1999, Society of Exploration Geophysicists, 389–398.

Bradford, J. H., W. P. Clement, and W. Barrash, 2009, Estimating porosity with ground-penetrating radar reflection tomography: A controlled 3-d experiment at the boise hydrogeophysical research site: Water Resources Research, **45**.

Brossier, R., S. Operto, and J. Virieux, 2009, Seismic imaging of complex onshore structures by 2d elastic frequency-domain full-waveform inversion: Geophysics, **74**, WCC105–WCC118.

Courant, R., K. Friedrichs, and H. Lewy, 1967, On the partial difference equations of mathematical physics: IBM journal of Research and Development, **11**, 215–234.

Dey, A., and H. Morrison, 1979, Resistivity modelling for arbitrarily shaped two-dimensional structures: Geophysical Prospecting, **27**, 106–136.

Doetsch, J., N. Linde, and A. Binley, 2010, Structural joint inversion of time-lapse crosshole ert and gpr traveltime data: Geophysical Research Letters, **37**.

Domenzain, D., J. Bradford, and J. Mead, 2020a, Joint inversion of full-waveform gpr and er data. part 1: Geophysics, **85**, https://doi.org/10.1190/geo2019–0754.1.

———, 2020b, Joint inversion of full-waveform gpr and er data. part 2: enhancing low

frequencies with the envelope transform and cross-gradients: Geophyiscs, **85**, doi: https://doi.org/10.1190/geo2019–0755.1.

Ellis, R., and D. Oldenburg, 1994, The pole-pole 3-d dc-resistivity inverse problem: a conjugategradient approach: Geophysical Journal International, **119**, 187–194.

Ernst, J. R., A. G. Green, H. Maurer, and K. Holliger, 2007, Application of a new 2d time-domain full-waveform inversion scheme to crosshole radar data: Geophysics, **72**, J53–J64.

Forte, E., and M. Pipan, 2017, Review of multi-offset gpr applications: Data acquisition, processing and analysis: Signal processing, **132**, 210–220.

Gallardo, L. A., and M. A. Meju, 2003, Characterization of heterogeneous near-surface materials by joint 2d inversion of dc resistivity and seismic data: Geophysical Research Letters, **30**.

Groos, L., M. Schäfer, T. Forbriger, and T. Bohlen, 2017, Application of a complete workflow for 2d elastic full-waveform inversion to recorded shallow-seismic rayleigh wavesworkflow for fwi of rayleigh waves: Geophysics, **82**, R109–R117.

Günther, T., C. Rücker, and K. Spitzer, 2006, Three-dimensional modelling and inversion of dc resistivity data incorporating topography—ii. inversion: Geophysical Journal International, **166**, 506–517.

Ha, T., S. Pyun, and C. Shin, 2006, Efficient electric resistivity inversion using adjoint state of mixed finite-element method for poisson's equation: Journal of Computational Physics, **214**, 171–186.

Keskinen, J., A. Klotzsche, M. C. Looms, J. Moreau, J. van der Kruk, K. Holliger, L. Stemmerik, and L. Nielsen, 2017, Full-waveform inversion of crosshole gpr data: Implications for porosity estimation in chalk: Journal of Applied Geophysics, **140**, 102 – 116.

Kochenderfer, M. J., and T. A. Wheeler, 2019, Algorithms for optimization: Mit Press.

Loke, M., 2006, Res2dinv ver. 3.55, rapid 2-d resistivity & ip inversion using the least-squares method: Software Manual, **139**.

Loke, M. H., and R. Barker, 1996, Rapid least-squares inversion of apparent resistivity pseudosections by a quasi-newton method 1: Geophysical prospecting, **44**, 131–152.

Marescot, L., S. P. Lopes, S. Rigobert, and A. G. Green, 2008, Nonlinear inversion of geoelectric data acquired across 3d objects using a finite-element approach: Geophysics, **73**, F121–F133.

Meles, G. A., J. Van der Kruk, S. A. Greenhalgh, J. R. Ernst, H. Maurer, and A. G. Green, 2010, A new vector waveform inversion algorithm for simultaneous updating of conductivity and permittivity parameters from combination crosshole/borehole-to-surface gpr data: IEEE Transactions on geoscience and remote sensing, **48**, 3391–3407.

Mwenifumbo, C. J., W. Barrash, and M. D. Knoll, 2009, Capacitive conductivity logging and electrical stratigraphy in a high-resistivity aquifer, boise hydrogeophysical research site: Geophysics, **74**, E125–E133.

Newman, G. A., and G. M. Hoversten, 2000, Solution strategies for two-and three-dimensional electromagnetic inverse problems: Inverse Problems, **16**, 1357.

Oldenborger, G. A., M. D. Knoll, P. S. Routh, and D. J. LaBrecque, 2007a, Time-lapse ert monitoring of an injection/withdrawal experiment in a shallow unconfined aquifer: Geophysics, **72**, F177–F187.

Oldenborger, G. A., P. S. Routh, and M. D. Knoll, 2007b, Model reliability for 3d electrical resistivity tomography: Application of the volume of investigation index to a time-lapse monitoring experiment: Geophysics, **72**, F167–F175.

Oldenburg, D. W., and Y. Li, 1999, Estimating depth of investigation in dc resistivity and

ip surveys: Geophysics, **64**, 403–416.

Pan, Y., L. Gao, and T. Bohlen, 2019, High-resolution characterization of near-surface structures by surface-wave inversions: From dispersion curve to full waveform: Surveys in Geophysics, **40**, 167–195.

Pica, A., J. Diet, and A. Tarantola, 1990, Nonlinear inversion of seismic reflection data in a laterally invariant medium: Geophysics, **55**, 284–292.

Pidlisecky, A., E. Haber, and R. Knight, 2007, Resinvm3d: A 3d resistivity inversion package: Geophysics, **72**, H1–H10.

Pidlisecky, A., and R. Knight, 2008, Fw2_5d: A matlab 2.5-d electrical resistivity modeling code: Computers & Geosciences, **34**, 1645–1654.

Pratt, R. G., C. Shin, and G. Hick, 1998, Gauss–newton and full newton methods in frequency–space seismic waveform inversion: Geophysical Journal International, **133**, 341–362.

Rumelhart, D. E., G. E. Hinton, and R. J. Williams, 1986, Learning representations by back-propagating errors: nature, **323**, 533.

Sasaki, Y., 1992, Resolution of resistivity tomography inferred from numerical simulation 1: Geophysical prospecting, **40**, 453–463.

Taillandier, C., M. Noble, H. Chauris, and H. Calandra, 2009, First-arrival traveltime tomography based on the adjoint-state method: Geophysics, **74**, WCB1–WCB10.

Tripp, A., G. Hohmann, and C. Swift, 1984, Two-dimensional resistivity inversion: Geophysics, **49**, 1708–1717.

Zhang, J., R. L. Mackie, and T. R. Madden, 1995, 3-d resistivity forward modeling and inversion using conjugate gradients: Geophysics, **60**, 1313–1325.

Zhou, Z., A. Klotzsche, T. Hermans, F. Nguyen, J. Schmäck, P. Haruzi, H. Vereecken, and

J. van der Kruk, 2020, 3d aquifer characterization of the hermalle-sous-argenteau test site using crosshole gpr amplitude analysis and full-waveform inversion: Geophysics, **85**, 1–74.

LIST OF TABLES

LIST OF FIGURES

located towards the beginning of the survey line. The dashed cyan line represents the water table depth as measured on site (1m deep). The solid cyan lines represent the borehole positions. Note the higher conductivity, sand filled paleo channel that deepens toward the river. The pixel size is 0.05m on each side.

10 Observed vs recovered ER data acquired at the BHRS.

11 Normalized recovered conductivities (red) and borehole neutron porosity (black) at borehole locations in the BHRS. The dashed gray line shows the cut-off for our appraised solution.

12 Recovered ER (with our method - in red) and capacitive conductivities (black) at borehole locations in the BHRS. The dashed gray line shows the cut-off for our appraised solution. Below the cut-off the solution returns to the reference model.

13 Comparison of our result in **a** and that of the commercial Res2DInv software in **b**. Results are shown in the computational domain without applying a topographic correction. The grid-size for **a** is 0.05m in width and length, while for **b** it is 0.5m long by 0.25m wide. The smallest possible horizontal spacing in Res2DInv is half of the receiver spacing (in this case 0.5m).

A-1 Algorithm for finding the 2.5D transformation weights $\boldsymbol{\omega}$.

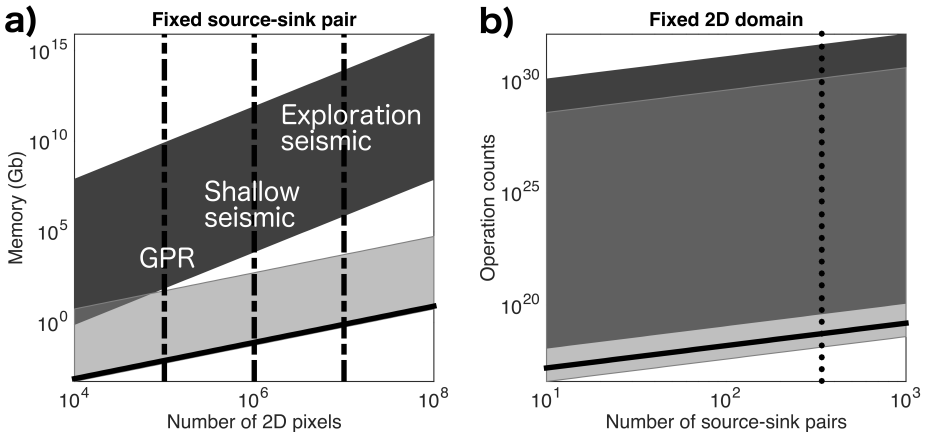

Figure 1: Efficiency in double-precision memory storage and operation count for a range of n_y copies of the 2D xz-domain: $1 \leq n_y \leq 10^4$. Solid black for both panels denotes our 2.5D method ($n_y = 4$). In **a** the memory needed to compute ER sensitivities as a function of domain size for a single source-sink pair. Dark gray denotes the Hessian of the objective function in 3D space. Light translucent gray denotes the 3D gradient descent using the adjoint method. The dashed lines mark the domain size needed for relevant GPR and Seismic surveys. In **b** the operation count for the fixed GPR domain size shown in **a**. Light translucent gray denotes the 3D gradient-descent using the adjoint method. Dark gray denotes the 3D adjoint conjugate-gradient method. The dotted line marks the number of source-sink pairs in our field experiment, of which there are 342.

–

		Domain size of		
		GPR	Shallow seismic	Exploration seismic
Method	3D Hessian	$8 \cdot 10^{9}$	$8 \cdot 10^{11}$	$8 \cdot 10^{13}$
	2D Hessian	$8 \cdot 10$	$8 \cdot 10^{3}$	$8 \cdot 10^{5}$
	3D adjoint gradient descent	$5 \cdot 10$	$5 \cdot 10^{2}$	$5 \cdot 10^{3}$
	2.5D adjoint gradient descent	$\mathbf{8 \cdot 10^{-3}}$	$\mathbf{8 \cdot 10^{-2}}$	$\mathbf{8 \cdot 10^{-1}}$
	2D adjoint gradient descent	$5 \cdot 10^{-3}$	$5 \cdot 10^{-2}$	$5 \cdot 10^{-1}$

Table 1: Double-precision memory in units of gigabytes needed for the ER sensitivities on the domains given by the GPR and seismic surveys depicted in Figure 1**a**. The values for the 3D Hessian and 3D adjoint gradient descent were taken with $n_y = 10^4$.

	Operation count
3D adjoint conjugate-gradient	$5 \cdot 10^{31}$
3D adjoint gradient-descent	$1 \cdot 10^{30}$
2D adjoint conjugate-gradient	$5 \cdot 10^{19}$
2.5D adjoint gradient-descent	$\mathbf{5 \cdot 10^{18}}$
2D adjoint gradient-descent	$1 \cdot 10^{18}$

Table 2: Operation count needed for computing ER sensitivities on the domain given by the GPR survey depicted in Figure 1**b**. The number of source-receiver pairs is taken from our field data example, of which there are 342. The values for the 3D adjoint conjugate-gradient scheme and 3D adjoint gradient descent were taken with $n_y = 10^4$.

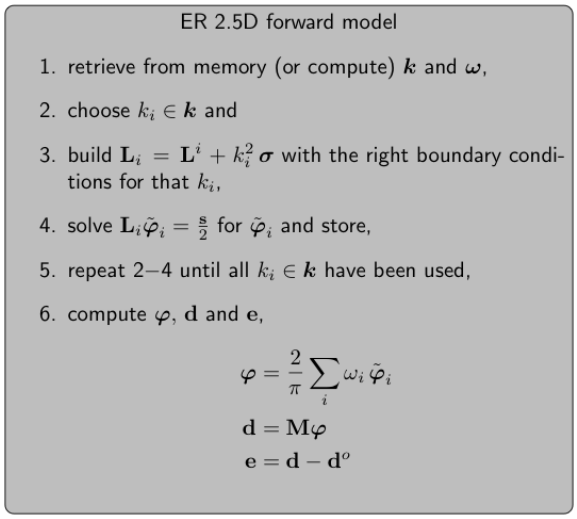

Figure 2: Algorithm for computing the 2.5D electric potential given a source $\mathbf{s}$ and conductivity $\boldsymbol{\sigma}$.

–

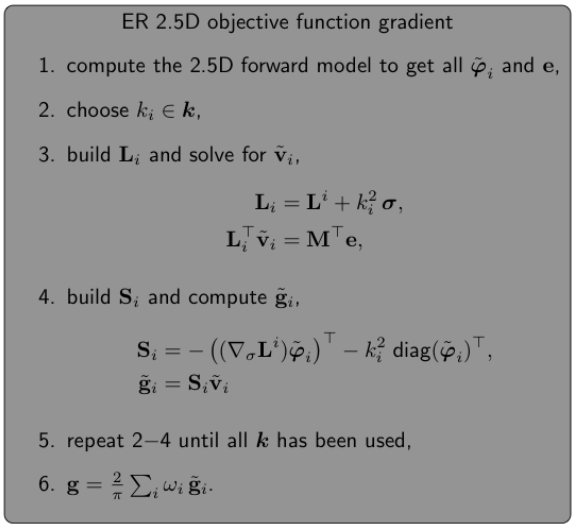

Figure 3: Algorithm for finding the 2.5D gradient $\mathbf{g}$.

–

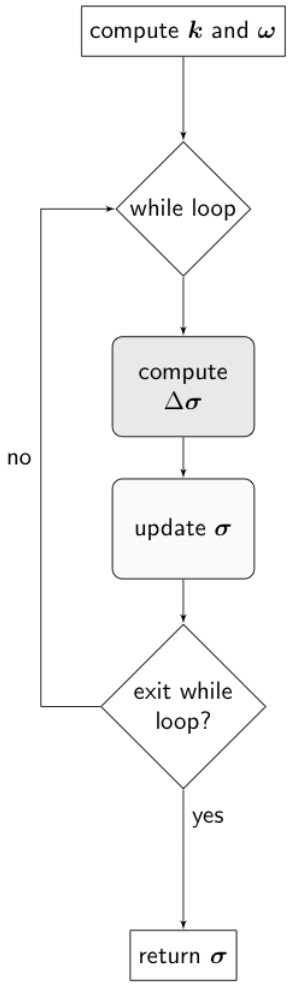

Figure 4: 2.5D inversion algorithm.

–

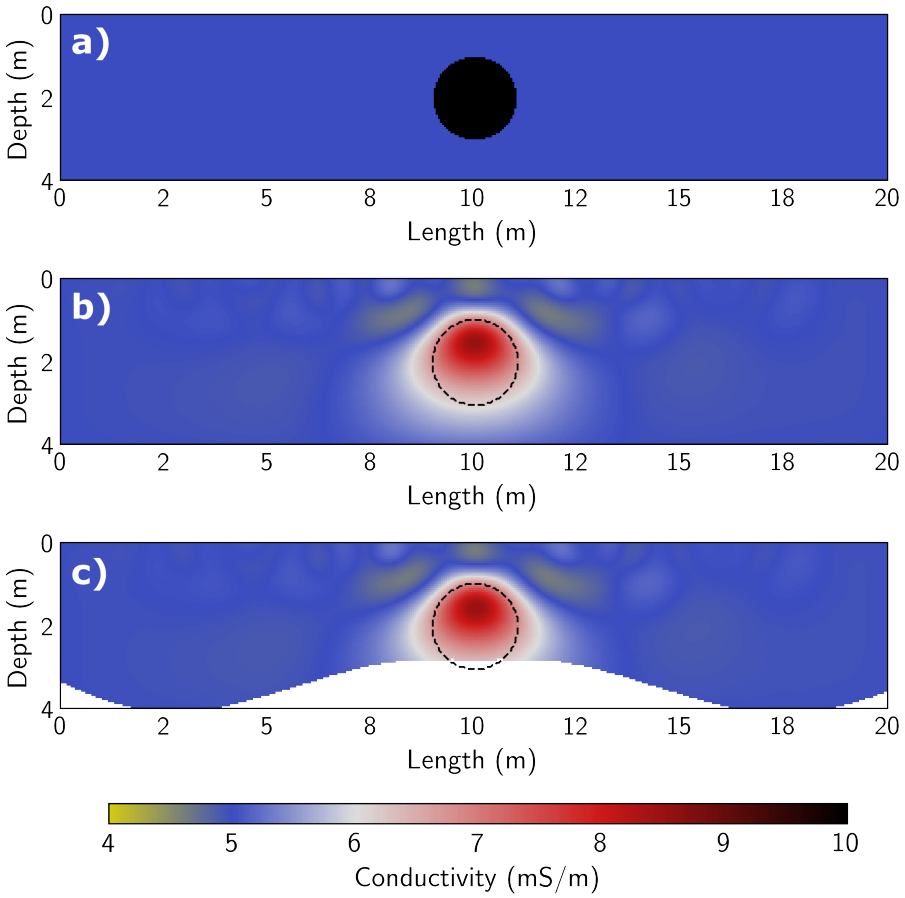

Figure 5: True **a**, recovered **b** and appraised **c** conductivity for the synthetic example. The dashed cyan line represents a borehole location. The dashed black line represents the contour of the cylinder. The pixel size is 0.05m on each side.

–

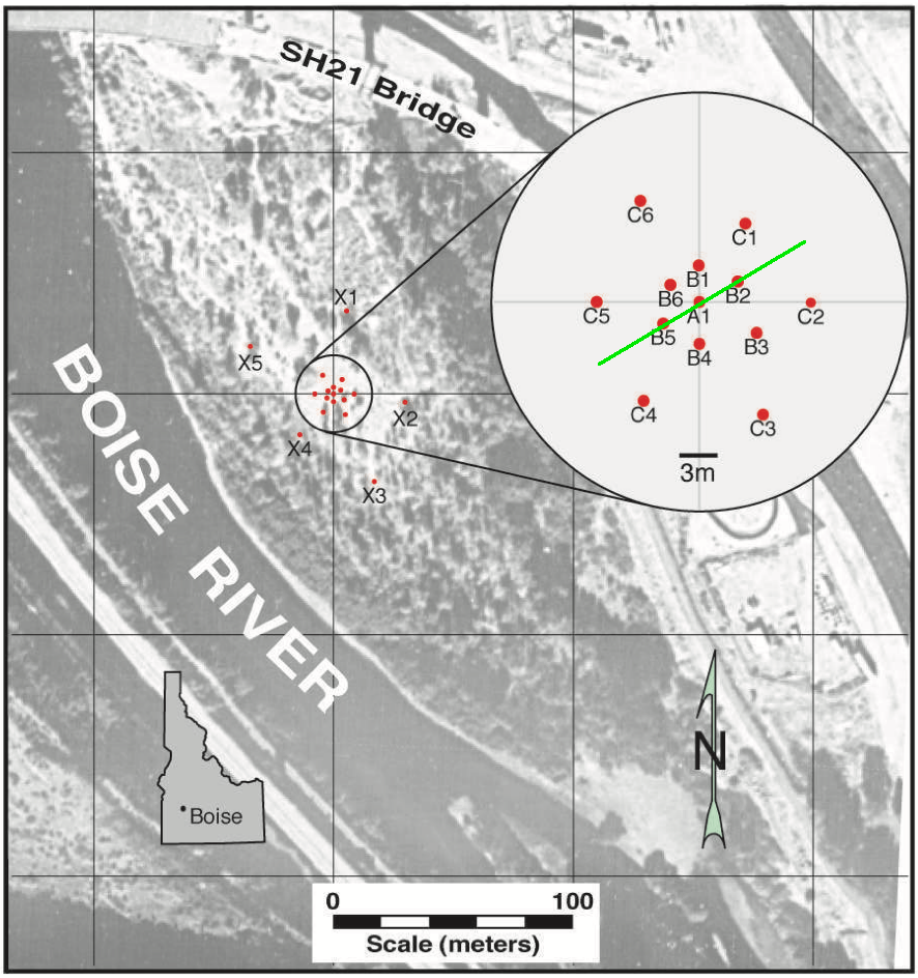

Figure 6: Geographic location of the Boise Hydrological Research Site (BHRS). The red dots denote the existing boreholes. Our survey line crossed boreholes B5, A1 and B2 as shown by the green line.

–

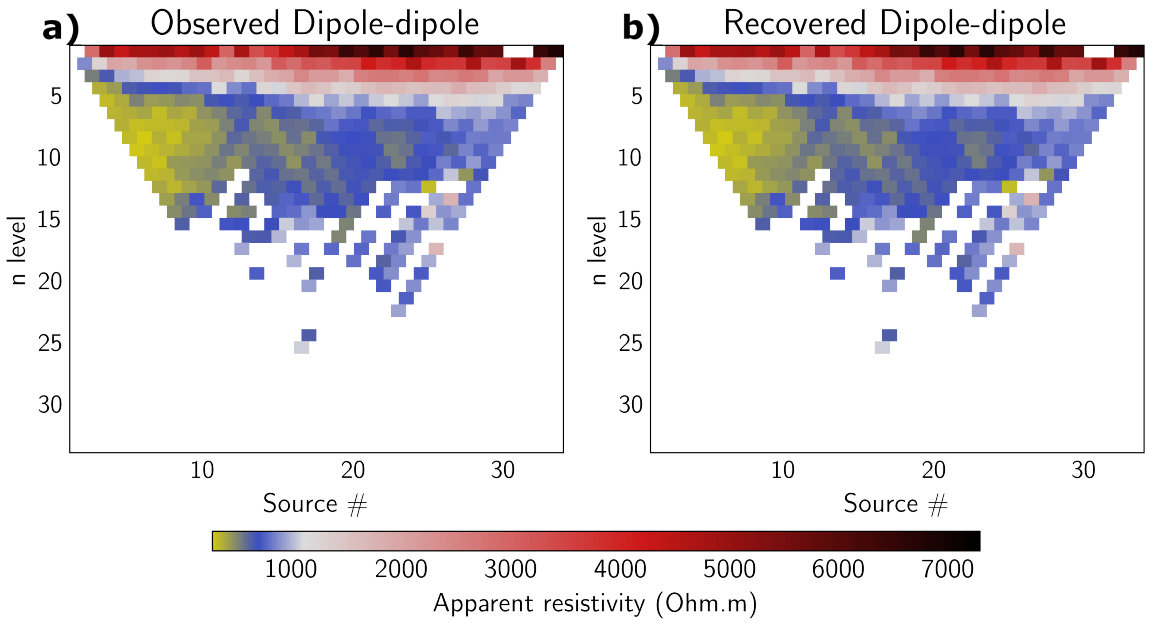

Figure 7: Dipole-dipole pseudo section with a-spacing equal to 1m from the BHRS.

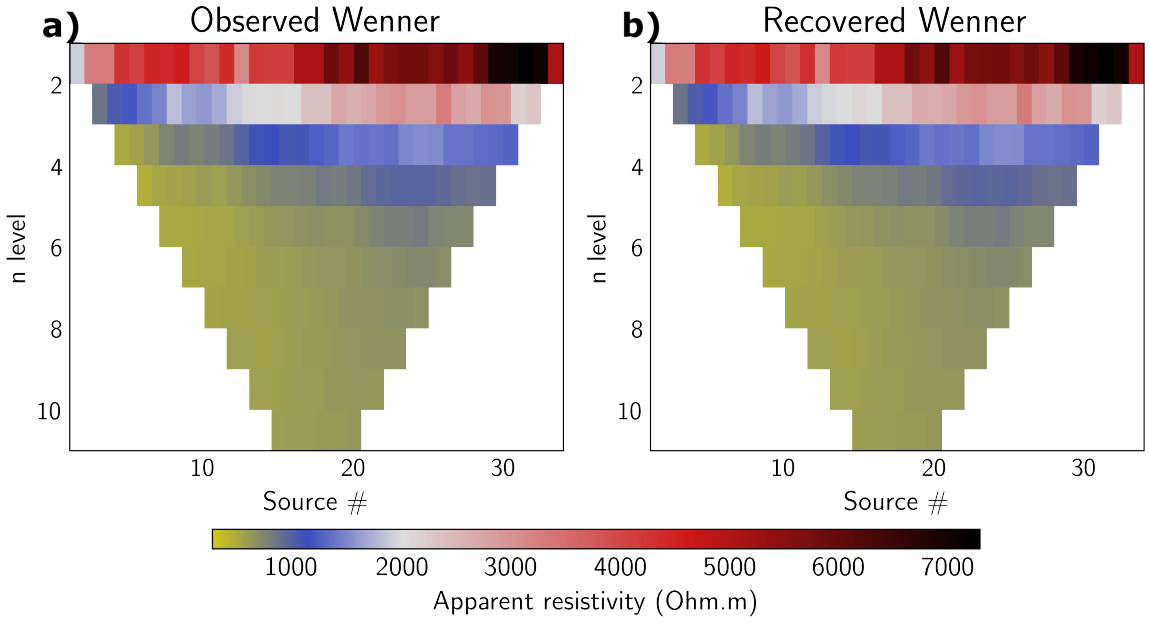

Figure 8: Wenner pseudo-section of the BHRS.

–

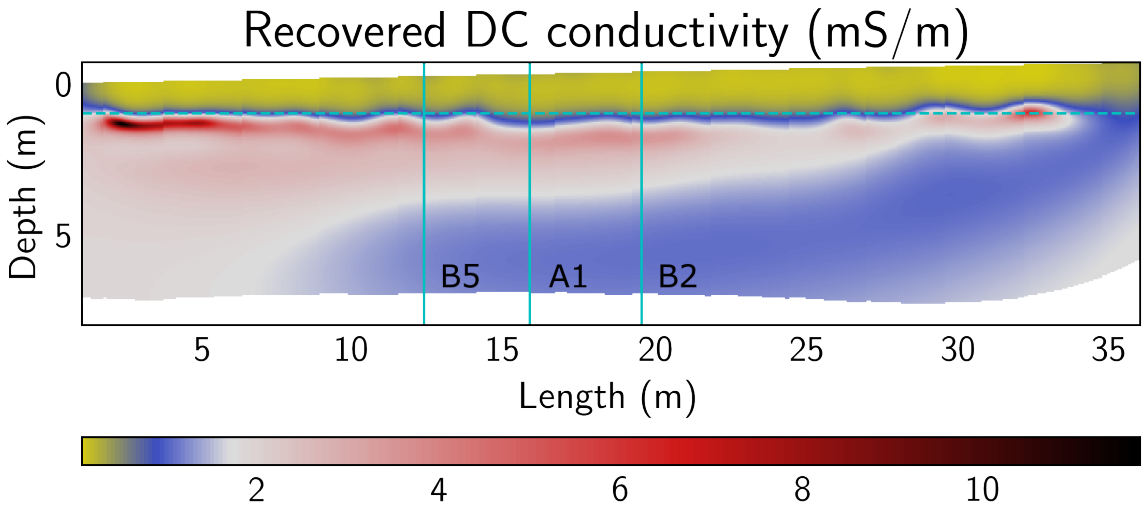

Figure 9: Recovered conductivity from the BHRS with topographic correction. The river is located towards the beginning of the survey line. The dashed cyan line represents the water table depth as measured on site (1m deep). The solid cyan lines represent the borehole positions. Note the higher conductivity, sand filled paleo channel that deepens toward the river. The pixel size is 0.05m on each side.

–

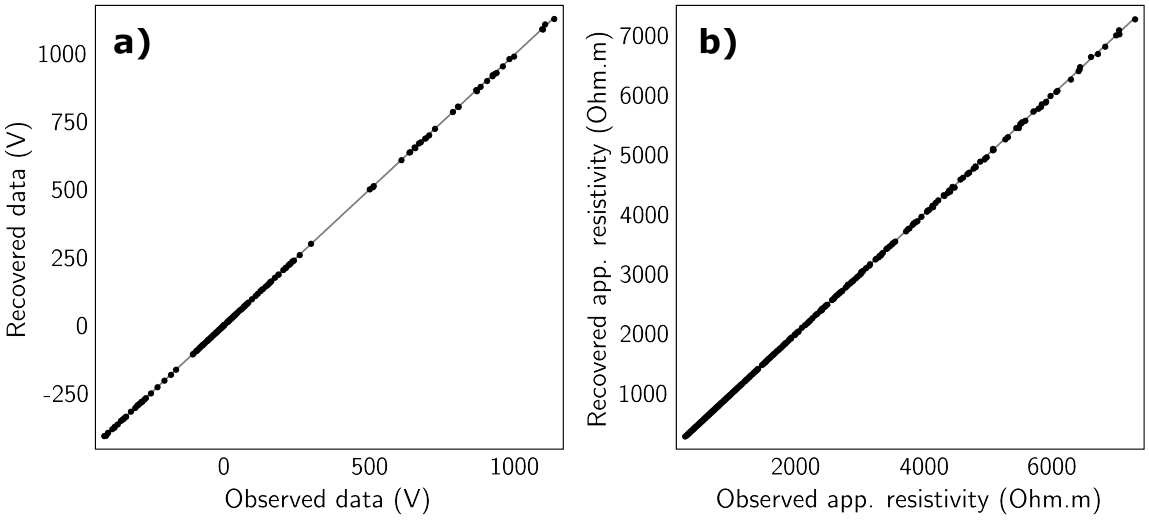

Figure 10: Observed vs recovered ER data acquired at the BHRS.

–

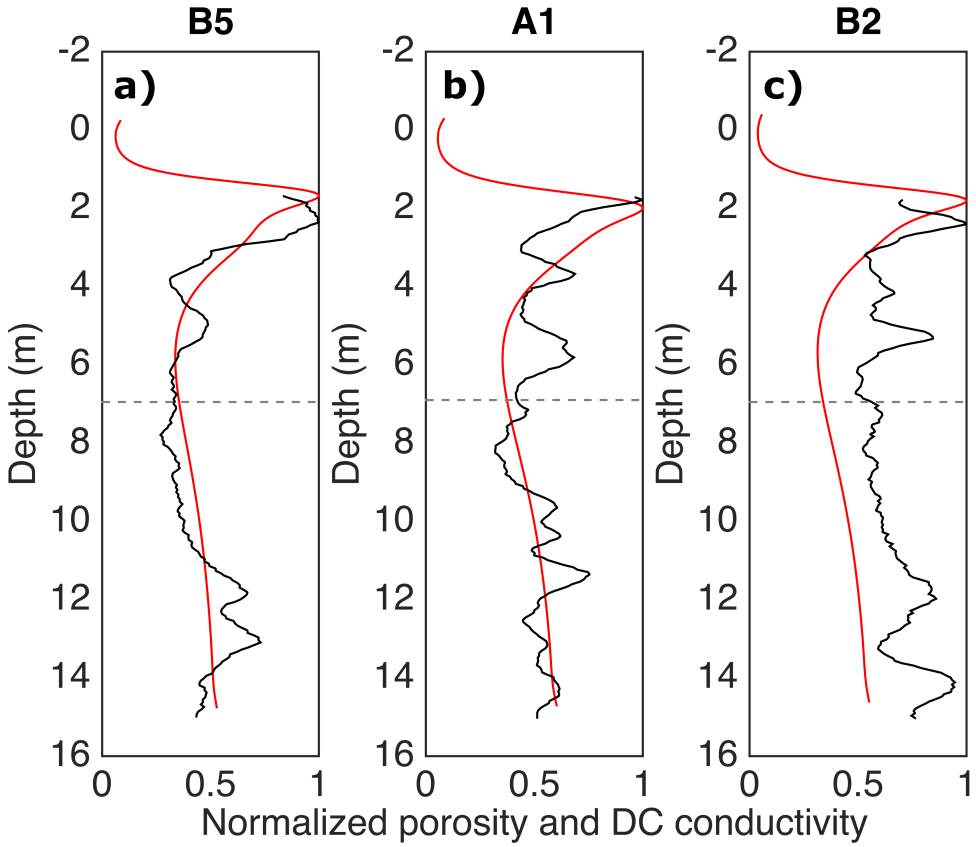

Figure 11: Normalized recovered conductivities (red) and borehole neutron porosity (black) at borehole locations in the BHRS. The dashed gray line shows the cut-off for our appraised solution.

–

	B5	**A1**	**B2**
m	1.8 ± 0.4	1.8 ± 0.3	1.5 ± 0.2
F_{ER}	11.9 ± 3	12.7 ± 4	13.5 ± 4
F_{ϕ}	14.3 ± 3	13.3 ± 4	13.4 ± 3

Table 3: Formation and cementation factor appraisal for each borehole using recovered conductivity and neutron porosities. Our results correlate well to a previous borehole ER survey at the same site up to a standard deviation of at most ± 1.

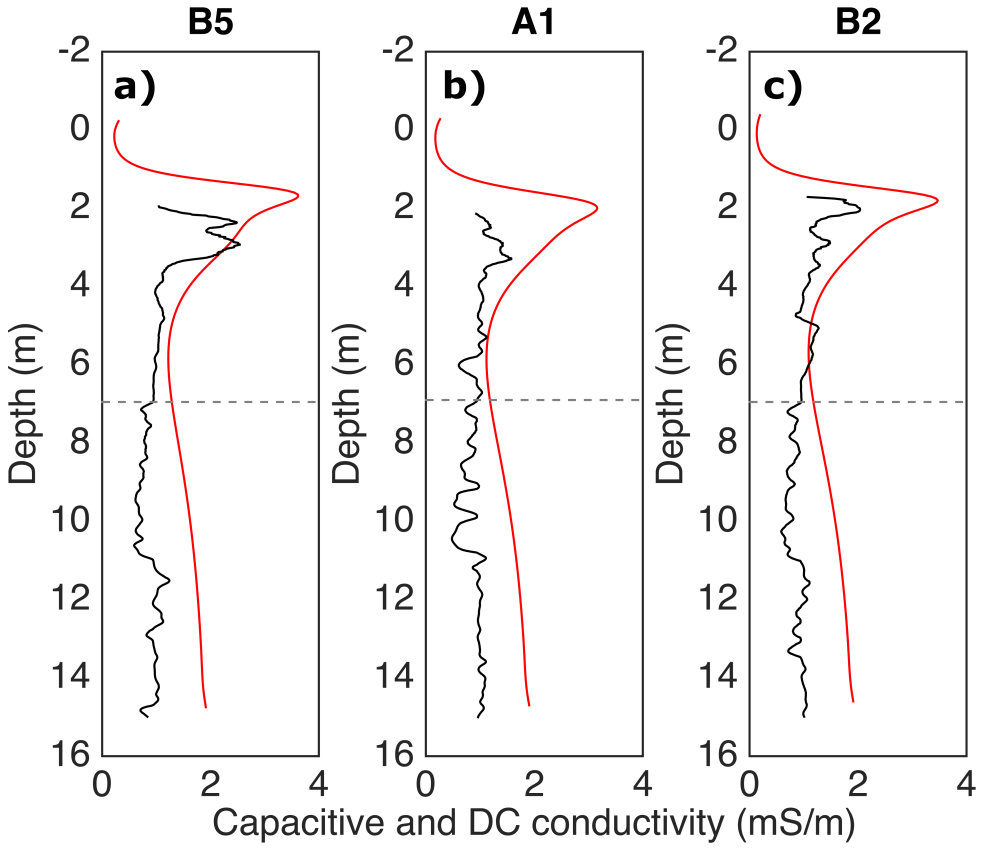

Figure 12: Recovered ER (with our method - in red) and capacitive conductivities (black) at borehole locations in the BHRS. The dashed gray line shows the cut-off for our appraised solution. Below the cut-off the solution returns to the reference model.

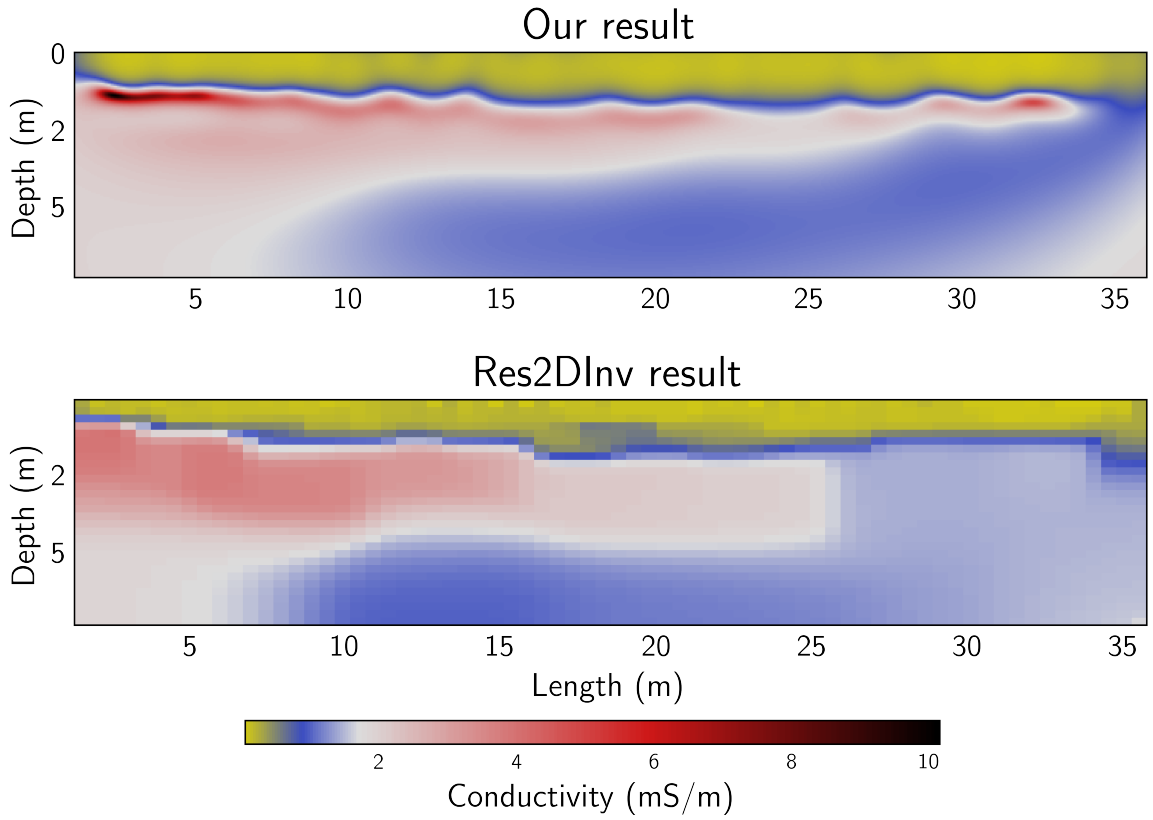

Figure 13: Comparison of our result in **a** and that of the commercial Res2DInv software in **b**. Results are shown in the computational domain without applying a topographic correction. The grid-size for **a** is 0.05m in width and length, while for **b** it is 0.5m long by 0.25m wide. The smallest possible horizontal spacing in Res2DInv is half of the receiver spacing (in this case 0.5m).

–

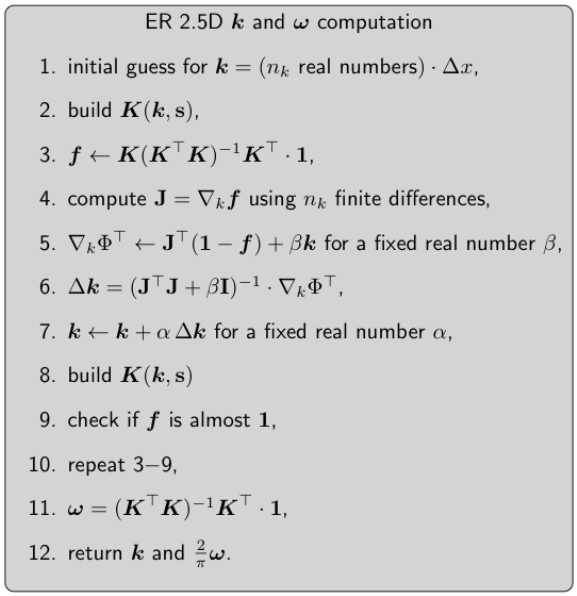

Figure A-1: Algorithm for finding the 2.5D transformation weights $\boldsymbol{\omega}$.

–